

Role of planar faults in martensite formation in nano-polycrystalline iron by molecular dynamics simulation

Karewar, Shivraj; Hidalgo, Javier; Sietsma, Jilt; Santofimia, Maria J.

DOI

[10.1007/s10853-022-07668-w](https://doi.org/10.1007/s10853-022-07668-w)

Publication date

2022

Document Version

Final published version

Published in

Journal of Materials Science

Citation (APA)

Karewar, S., Hidalgo, J., Sietsma, J., & Santofimia, M. J. (2022). Role of planar faults in martensite formation in nano-polycrystalline iron by molecular dynamics simulation. *Journal of Materials Science*, 57(37), 17678-17699. <https://doi.org/10.1007/s10853-022-07668-w>

Important note

To cite this publication, please use the final published version (if applicable).
Please check the document version above.

Copyright


Other than for strictly personal use, it is not permitted to download, forward or distribute the text or part of it, without the consent of the author(s) and/or copyright holder(s), unless the work is under an open content license such as Creative Commons.

Takedown policy

Please contact us and provide details if you believe this document breaches copyrights.
We will remove access to the work immediately and investigate your claim.



Role of planar faults in martensite formation in nanopolycrystalline iron by molecular dynamics simulation

Shivraj Karewar^{1,*} , Javier Hidalgo^{2,3,*}, Jilt Sietsma², and Maria J. Santofimia²

¹Department of Mechanical Engineering, Eindhoven University of Technology, P.O. Box 513, 5600 MB Eindhoven, The Netherlands

²Department of Materials Science and Engineering, Delft University of Technology, Mekelweg 2, 2628 CD Delft, The Netherlands

³DYPAM Research Group, ETSII-INEI, Universidad de Castilla La Mancha, Avda. Camilo Jose Cela s/n, 13071 Ciudad Real, Spain

Received: 23 February 2022

Accepted: 23 July 2022

Published online:

1 October 2022

© The Author(s) 2022

ABSTRACT

The martensitic transformation in pure Fe and its alloys has been studied over many decades. Several theoretical models have been proposed to describe the atomic motion that leads to the fcc-to-bcc martensitic transformation. However, such models do not account for the effect of pre-existing planar defects such as twin boundaries and stacking faults, present in the high-temperature austenite phase prior to the transformation process. This work systematically studies the role of nano-spaced planar faults with different inter-spacing on the martensitic transformation using molecular dynamics simulations. Research shows that the investigated planar defects affect the nucleation and growth mechanisms during martensite formation, the morphology of the resulting microstructure, the specific atomic path leading to the phase transformation, and the martensite start temperatures. Martensite variants were identified by the analysis of the atomic shears and slip systems during the transformation process. A crystallographic analysis is done to explain the existence of different shear mechanisms of martensite transformation at different locations in the fcc austenite. The present investigation provides fundamental insights into the martensitic transformation process in presence of pre-existing planar defects and can be applied to other material systems, e.g., Fe alloys.

Handling Editor: Avinash Dongare.

Address correspondence to E-mail: s.v.karewar@tue.nl; karewar1@gmail.com; J.HidalgoGarcia@tudelft.nl; jhidalgophd@gmail.com

Introduction

The production of steel commonly implies plastic deformation of austenite and the development of a high density of defects in this phase. Depending on the stacking fault energy (SFE) of the alloy at the deformation conditions, dislocations, stacking faults, and twins are formed in austenite [1–5]. Wang et al. [4] and Lu et al. [5] observed the formation of nanotwinned face centered cubic (fcc) austenite grains during plastic deformation and thermal annealing process in Fe-Mn alloy with low SFE. The average twin/lamella thickness observed in their work was as low as 5 nm. Such nanotwinned austenite grains are thermally more stable than nanograins and led to an increased strength-ductility synergy in the specimen. Hence, it is important to consider the effect of such nanoscale planar defects on the martensitic phase transformation mechanisms as well. Our comprehension of the exact underlying mechanisms during the nucleation and growth of martensite in presence of such defects is very limited. This understanding will enable, e.g., to engineer the defects in austenite for control of the martensite transformation, the microstructure, and the resulting properties. Austenite grain size can also be tailored to dictate martensitic transformation. Reducing austenite grain sizes below the micrometer is gaining attention and has been proven feasible after severe plastic deformation and subsequent intercritical or full annealing treatments [6, 7]. The specific characteristics of martensite formation in such fine grains are also not clear. Although experimental observations are available in the literature, they rely on the final microstructures for the assessment of mechanisms and are susceptible to confounding factors. In experimental analysis, one has to trace back the atomic displacements that could lead to the transformation. This trace-back process does not consider the effects of planar defects (stacking faults (SFs) or twin boundaries (TBs) or grain boundaries (GBs)), and therefore could result in an incomplete analysis [8, 9]. The diffusionless and sudden formation of martensite crystals at speeds close to the speed of sound makes direct experimental observations of martensite formation very challenging. Besides, it is difficult to observe and analyze defects in the high-temperature austenite phase experimentally. The advent of multiscale modeling techniques in

combination with advanced experimental tools is empowering our comprehension of the martensitic transformation. In this regard, molecular dynamics (MD) simulations provide powerful tools to analyze the atomistic aspect of phase transitions and also enable the *in situ* observation of the atomic shears leading to the transformation.

The diffusionless character of martensite formation implies a coordinated movement of atoms maintaining certain orientation relations with the parent austenite phase. The orientation relationship between martensite and prior austenite is typically close to that predicted by Kurdjumov and Sachs (K-S) [10] or Nishiyama–Wassermann (N-W) models [11]. These models, and also the phenomenological theory of martensite transformation [8], are lattice transformation models that consider perfect unit cells of fcc austenite and body centered cubic (bcc) martensite to predict the transformation path. However, the theoretical models do not consider the role of pre-existing planar faults on the atomic motions leading to the transformation and therefore might not predict accurately the transformation pathways. Only Bogers–Burgers–Olson–Cohen model [12, 13] considers the nucleation in presence of pre-existing SFs. The inadequacies of these models are described by Bhadeshia and Wayman who emphasized that phenomenological models mathematically relate all crystallographic features between austenite and martensite, although it does not provide thorough information about the transformation mechanisms [14].

Moreover, it is difficult to observe the martensite nucleation experimentally. The activation energy for martensite heterogeneous nucleation is much less than homogeneous nucleation, and thus homogeneous nucleation is believed to not be possible [15, 16]. Nonetheless, several works evaluated the activation energy of the homogeneous nucleation event in Fe alloys and posed that the homogeneous nucleation of martensite can be stimulated by thermal fluctuation [17, 18]. Furthermore, computer simulations have demonstrated the possibility of homogeneous nucleation [19]. The heterogeneous nucleation of martensite is observed at GBs, triple junctions, dislocations, TBs, and SFs [2, 20–23]. The effect of dislocations on martensite formation is relatively complex and controversial. Dislocations are commonly believed as probable nucleation sites after most prevailing Bogers–Burgers–Olson–Cohen

model for martensite nucleation [12, 13]. This model hypothesizes that a martensite embryo may form after the separation of dislocations into partial dislocations and the intersecting shear of the two arrays of partial dislocations. He et al. [24] suggested that the presence of geometrically necessary dislocations contiguous to the austenite GB increases martensite start temperature (M_s) when low plastic strain is applied to prior austenite. Song and De Cooman [25] showed that the intrinsic grain boundary dislocations are favorable nucleation locations. Nonetheless, it is a common belief that dislocations generated at the nuclei/austenite interface can glide to extend the interface and cause the growth of martensite [15, 26]. Otte [27] concluded that SFs are not likely nucleation sites of martensite, although SFs can accommodate the first sequence of shears proposed by K–S. Later studies [8, 28] pointed out that the SFs formed during cooling may provide the nucleation defects required in the Olson and Cohen model. This postulate was made quite arbitrarily, due to the absence of direct and thorough experimental observations.

It is generally accepted that the accommodation of shape strain of transforming martensite by plastic strains in parent austenite is a crucial step in the martensite growth process. Dislocations are necessary to initiate the development of plastic strains in the austenite. However, a high dislocation population can have the opposite effect due to a strengthening effect. It is well credited that reducing the austenite grain size favors the stabilization of austenite against martensitic transformation. The M_s temperature abruptly decreases as the prior austenite grain size is reduced below several tens of micrometer [29–31]. Ansell and co-workers [32, 33] determined that this effect is intrinsically related to the grain-size influence on the resistance of the austenite against plastic deformation. Martensite transformation can even be completely suppressed below a critical austenite grain size, typically in the range of several tens of nanometer [34, 35]. Twins divide the parent austenite grain into different subgrains with characteristic crystallography. Hence, it is reasonable to assume that the increase of twin density will decrease the M_s due to a reduction in the grain size, but a clear effect of the presence of twins in the austenite phase on the martensitic transformation is not yet known. The dislocation motion can be blocked by the SFs and nano twins, which would contribute to austenite strengthening [36, 37]. It follows that the presence of

these defects should hinder the austenite to martensite transformation. However, there is a lack of experimental evidence that relates the twin or stacking fault density and spacing in austenite with the transformation mechanisms and M_s temperature.

During the formation of martensite, crystallographic variants of the martensite form a complex hierarchical structure with domains in various length scales, ranging from nanometers to micrometers, to mutually compensate for their transformation strains. Takaki et al. [35] suggested that decreasing austenite grain size hinders the multi-variant transformation and can lead to the inhibition of the martensitic transformation in metastable austenite. Hence, prior austenite grain size also affects the hierarchical microstructure of martensitic steels, dictating the size and distribution of different substructures [30, 38]. Crystal sizes at the nanoscale can create different martensite transformation pathways and thus microstructures that are different from those of coarse crystals [39]. The martensite formed at TBs typically exhibits a chevron morphology consisting of the assembly of two martensite lenticles that maintain a K–S relationship with both twin-related parent crystals [21, 40].

In this work, the formation of martensite is systematically studied with and without the presence of planar defects in fcc austenite, such as TBs and SFs, by MD simulations in pure Iron. Different interspacing of planar defects are introduced in nanoscale austenite to understand their effect on the microstructural features of austenite, which eventually affects the martensitic transformation mechanisms. The MD simulations used in this work enable the observation of the atomic motion as the transformation progresses and yield detailed information about the transformation mechanisms, which is difficult experimentally. It also allows analyzing the lattice models of transformation in presence of these defects. The local atomic arrangements in fcc austenite which lead to the activation of a particular type of transition mechanism are also analyzed.

Simulation method

The Large-scale Atomic/Molecular Massively Parallel Simulator (LAMMPS) was used to carry out

MD simulations [41]. The Open Visualization Tool (OVITO) [42] was used for the visualization and the analysis of the microstructure. The in-built analysis methods in OVITO such as the adaptive common neighbor analysis (a-CNA) [43], displacement calculation modifier, and the polyhedral template matching [44] method were used. The atomic displacements were shown at the heads of the atoms, and they represent the original positions from where the atoms were displaced. These are calculated with respect to the previous configuration (1 ps difference) and are scaled by 2.5 for better visualization. The fcc austenite nano-polycrystalline simulation systems with and without the pre-existing defects were created by an open-source software Atom/Molecule/Material Software Kit (Atomsk) [45] using the Voronoi tessellation method. This method has been widely used to create atomistic simulation geometries and gives results that agree well with the experiments.

The selection of interatomic potential is crucial for MD studies. Engin et al. [46], and Meiser and Urbassek [47] concluded that only the Meyer–Entel potential [48], among the different types of potentials in literature, is capable to describe both the bcc-to-fcc and fcc-to-bcc transformation. Cuppari et al. [49] used an analytical bond order potential [50] to conclude that this potential showed no fcc-to-bcc transformation during cooling (the fcc was stable and it did not transform to bcc). In the current work, it is important to have a qualitatively good approximation of the SFE, as it influences the stability of the planar faults studied in this work. The SFE of Meyer–Entel embedded atom model (EAM) potential along the $\{111\}\langle 112 \rangle$ slip system is -54 mJ/m^2 [20]. Even though the EAM formalism does not consider the magnetism explicitly, this value approximates better to the SFE of paramagnetic fcc of -105 mJ/m^2 compared to the -415 mJ/m^2 of non-magnetic fcc, both calculated by first-principles studies [51, 52]. The negative SFE in both Meyer–Entel potential and first principles points to a spontaneous formation of SFs and TBs in the fcc phase at high temperature, also observed experimentally during bcc to fcc transformation on heating [3]. This is crucial for the present study because the energetics of the planar defects will dictate their stability in the fcc phase, and in turn, will affect the atomistic transformation pathways. Considering all these facts, in particular the qualitative

agreement of the SFE value with the first principles data, the Meyer–Entel potential [48] is used in this study to assess the influence of planar defects on the transformation in nanograin sized crystals. This potential has been used in several simulations [19, 20, 53–58] to describe the martensitic transformation.

This potential, however, does not take into account the magnetic effects. Although this deficiency affects the relative stability of the two phases, it can be presumed that it does not affect the transformation mechanisms [59], since it correctly describes the transition from bcc-to-fcc and vice-versa. This approach is in line with existing lattice transformation models that also do not consider the magnetism or effect of alloying elements, and still provide a good comprehension of the mechanisms that are observed and validated experimentally. The austenite lattice constant for the Meyer–Entel potential is 3.686 \AA [60], which is higher than that extrapolated from experimental measurements of 3.570 \AA [61]. This makes the atomic volume of fcc greater than that of bcc and thus, contrary to conventional observations, a volume increase occurs during bcc-to-fcc transformations and a decrease during fcc-to-bcc transformation. As discussed in the works of Song et al. [25] and Karewar et al. [20], the fcc-to-bcc transformation in Fe is mainly dictated by the qualitative comparisons of the lattice constant of the individual phases (lower lattice constant for bcc phase and higher for fcc), and the atomic shear directions, both of which match qualitatively with the experiments. Also, qualitatively the correct magnitudes of SFE and the trends of pressure evolution during transformation along different paths are particularly of importance in the present scenario where we expect planar defects to play an important role during the transition. As discussed earlier, the SFE is in good agreement with first-principles work, and as discussed by Sandoval et al. [57], the Meyer–Entel potential shows qualitatively correct pressure evolution along K–S and N–W shear paths compared to the Bain transformation path. Therefore, this discrepancy does not affect the transformation mechanisms. The discrepancy of the atomic volume will lead to the opposite nature of the atomic stresses and pressure evolution in the simulation system, compared to the experiments, during the transformation, i.e., compressive instead of tensile and vice-versa.

We also performed representative simulations using a modified embedded atom method (MEAM) interatomic potential [62] to check that the results presented here are reproduced with another interatomic potential. For this potential, the fcc austenite phase is not stable even at the higher temperature of 1200 K, it transforms to the bcc phase immediately at this temperature during the equilibration process. Therefore, the same strategy of cooling from 1200 to 10 K cannot be used for this potential. For MEAM potential, the sample is minimized first and then isothermal annealing was carried out at a lower temperature of 100 K. The martensitic transformation is then tracked as a function of time. The M_s temperature cannot be evaluated in this way, but the transformation mechanisms can be compared with the results from the EAM potential.

Simulation systems with the dimensions of $600 \times 400 \times 20.9 \text{ \AA}^3$ were used. The total number of atoms varied between 398550 and 398900 depending on the planar defects present in a given simulation system. The preferentially oriented grains with the Z-axis parallel to $[\bar{1}10]$ were used. The Z-axis is the tilt axis and random orientations were assigned to each grain. Periodic boundary conditions were used in all directions. This type of geometry has been used previously by Song and Hoyt [63] as it allows having larger grain sizes in the XY plane and creates infinitely long grains along the Z direction. It simplifies the creation and visualization of the planar defects in the fcc austenite phase. Additionally, it makes it easier to analyze the observed transition mechanisms without any additional complications that might be present in a 3D simulation system with randomly oriented grains, e.g., easier tracking of the atomic movements during the transformation process. In the future, such simulations in a system with randomly oriented grains or even a Fe alloy system could be carried out. The simulation systems consist of six grains with an average grain size of 25.5 nm. The grain sizes are calculated as an average of major axes in a hexagonal grain, the values are then averaged over six grains.

The exact parameters for the three configurations used in this work are given in Table 1, and these configurations are:

- Defect free (NPC_0): fcc austenite nano-polycrystalline simulation system without pre-existing planar defects such as TBs or SFs,
- Twin boundaries (NPC_{TB}): fcc austenite nano-polycrystalline simulation system with pre-existing TBs,
- Stacking faults (NPC_{SF}): fcc austenite nano-polycrystalline simulation system with pre-existing SFs.

The distance between TBs (λ_{TB}) and SFs (λ_{SF}) in configurations with pre-existing TBs and SFs, respectively, is changed as given in Table 1. The centers of the grains in each configuration are also changed to obtain two different grain distributions with a variable nature of the GBs and also the misorientations between each grain. It allows us to study the effects of random statistics of GBs and their misorientations on the martensitic transformation. The grain centers are given in the third and fourth columns of Table 1 as fractional coordinates of simulation system size along each direction. These spatial coordinates of grain centers were used to create six grains for all three configurations.

A few representatives of these simulation volumes are shown in Fig. 1a–d. The atomic colors represent a-CNA. Figure 1a, b shows the configurations without defects and with pre-existing TBs with grain centers 1. The misorientation angles between some of the GBs are shown in (a), and the grain numbers are shown in (b). The same grain numbers are used in the rest of the paper. A close-up view, in subfigure (b), at the triple junction of grains 1–5–6 is shown. The single layer of red atoms with a hexagonal close packed structure (hcp) represent TBs in this configuration, and the distance between them is indicated as $\lambda_{TB} = 27.6 \text{ \AA}$. “M” indicates the original matrix orientation which is the same as in configuration without defects, and “T” indicates the twinned region. The area marked by orange rectangles in Fig. 1a, b will be discussed in the next Fig. 2. Configuration with pre-existing SFs with grain centers 2 is shown in Fig. 1c. A zoomed-in view of the triple junction GB is shown in the bottom row. The two layers of red atoms with hcp stacking represent the SF, and the distance between them is indicated as $\lambda_{SF} = 27.9 \text{ \AA}$. Figure 1d shows the perspective view of the configuration with pre-existing TBs with $\lambda_{TB} = 55.3 \text{ \AA}$. The $Z \parallel [\bar{1}10]$ axis marked here is the same for all grains and represents their rotation axis.

The simulation systems are first minimized at 0 K to remove high energy atomic environments and to

Table 1 Details of various configurations used in this study

Configurations	Defect spacing (λ_{TB} or λ_{SF} , Å)	Grain Centers 1 (*lx, *ly, *lz), Å	Grain Centers 2 (*lx, *ly, *lz), Å
NPC_0	No pre-existing planar defects	(1) 0.1, 0.88, 0.5;	(1) 0.15, 0.85, 0.5;
NPC_{TB} Pre-existing TBs	λ_{TB} 27.6, 55.3, 80.8	(2) 0.48, 0.025, 0.5;	(2) 0.5, 0.07, 0.5;
NPC_{SF} Pre-existing SFs	λ_{SF} 27.9, 53.2, 78.7	(3) 0.8, 0.85, 0.5;	(3) 0.7, 0.4, 0.5;
		(4) 0.82, 0.2, 0.5;	(4) 0.85, 0.1, 0.5;
		(5) 0.5, 0.5, 0.5;	(5) 0.45, 0.45, 0.5;
		(6) 0.13, 0.2, 0.5	(6) 0.17, 0.19, 0.5

λ represents the distance between the planar defects for configurations with pre-existing TBs (NPC_{TB}) and SFs (NPC_{SF}). The locations of the centers of six grains expressed as factors of simulation box dimensions along each direction are given in the third and fourth columns: the grain numbers are indicated in round brackets () and the corresponding spatial coordinates are given next to it. These spatial coordinates (of grain centers) were used to create six grains for all three configurations with two different coordinates of grain centers. An example is shown in Fig. 1b

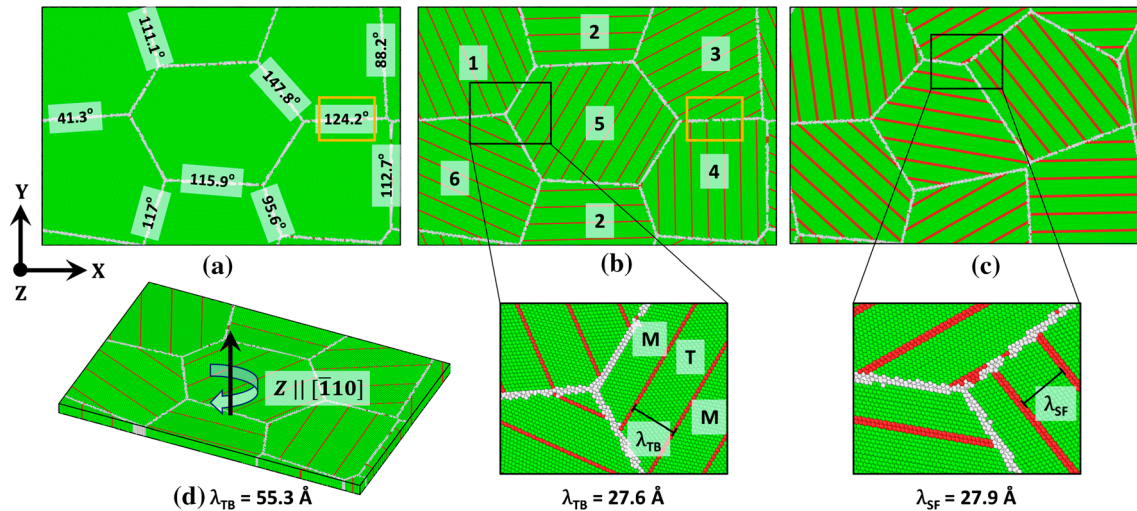


Figure 1 Some representative simulation systems used in this study. **a** Configuration NPC_0 : fcc nano-polycrystalline simulation system aggregate without planar defects. The angles indicate the misorientations between the two grains, **b** Configuration NPC_{TB} for grain centers 1 with pre-existing TBs ($\lambda_{TB} = 27.6$ Å). **c** Configuration NPC_{SF} for grain centers 2 with pre-existing SFs ($\lambda_{SF} = 27.9$ Å). The zoomed-in views of the

configurations at the marked rectangle in **b**, **c** are shown in the bottom row. **d** NPC_{TB} for grain centers 1 with pre-existing TBs ($\lambda_{TB} = 55.3$ Å). The axis indicates the rotation axis for all grains. The atomic colors are as per a-CNA: green—fcc, blue—bcc, red—hcp, gray—unidentified or atoms at the GBs. M = matrix, T = twin.

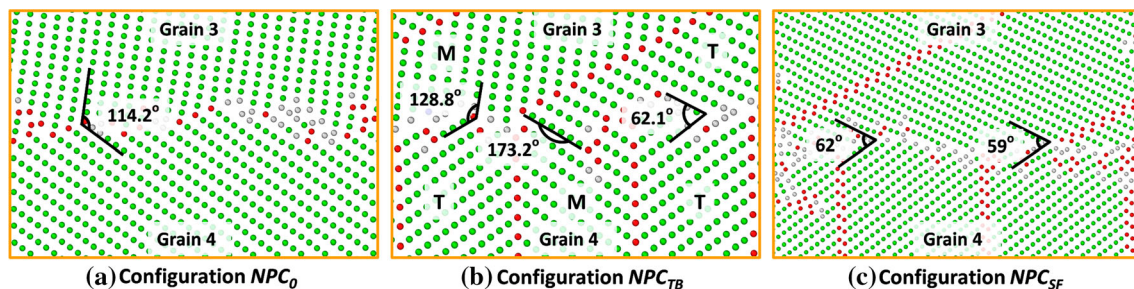


Figure 2 The close-up views of the GBs for different configurations along with the corresponding misorientations. M = matrix, T = twin.

reduce high system stresses produced by the polycrystal generation scheme. After that, the simulation system is equilibrated at 1200 K for 100 ps using the NPT ensemble. At this temperature, a stable fcc phase is observed for Meyer–Entel potential and in experiments also. Each dimension of the simulation system was allowed to equilibrate independently so that the pressure reduces to less than ± 20 MPa along each direction. For each configuration and each grain center, three random initial velocities of atoms were used to equilibrate the samples. The use of random velocities generates different velocity trajectories during cooling. The simulation system with a stable fcc phase is then cooled to 10 K at a cooling rate of 1 K/ps using the NPT ensemble. The total cooling time was 1.19 ns for all simulation systems. A cooling rate of 1 K/ps was found to be reasonable in previous MD simulations of martensitic phase transformations [20, 53] for obtaining a representative number of temperature conditions and simulation times. A higher cooling rate does not induce martensitic transformation when using the Meyer–Entel interatomic potential [20, 53].

Results

The zoomed-in views of the state of the GBs after equilibration for the three configurations with grain centers 1 are shown in Fig. 2a–c. The monolayer of atoms at the GB between grains 3 and 4 (as marked by the orange rectangle in Fig. 1a, b) is shown to compare the atomic arrangement in different configurations. The misorientation is calculated by measuring the angle between the $\langle 110 \rangle_{\text{fcc}}$ directions across the GBs as shown in these figures. The misorientation angle for configuration without defects is 114.2° . This misorientation stays the same throughout the GB between grains 3 and 4 in this configuration.

The misorientation angles at the GB for configuration NPC_{TB} , with pre-existing TBs, are shown in Fig. 2b. The line of red atoms represents the TBs in this configuration (identified as hcp stacking by a-CNA). The part of the grain across the TBs are mirror images of each other. The part of the grain marked as “M” indicates the original matrix or grain orientation—the atomic arrangement here is similar to that of configuration without defects. The “T” indicates the twinned part of the grain and is a mirror image of the previous block. On the left side of this figure, the

misorientation angle has been changed to 128.8° compared to 114.2° in configuration NPC_0 , without defects, because of the twinned region in the bottom grain. In the middle part, there is a minimal mismatch of 173.2° between the two grains. This mismatch is accommodated as stacking faults and the rest of the area is identified as the coherent fcc region by a-CNA (e.g., see the GB between grain 3 and 4 in Fig. 4a for $\lambda_{TB} = 80.8 \text{ \AA}$). The rest of the atoms in this region are identified as fcc by the a-CNA algorithm. On the right-hand side, the misorientation angle is 62.1° . Thus, the introduction of TBs in configuration NPC_{TB} , with pre-existing TBs, modifies the local substructure of the prior austenite grain and also the local atomic arrangements across the length of the GB between grain numbers 3 and 4. The same applies to the other GBs in this configuration.

The SFs create local atomic shear and change the order of atomic arrangement at the location of SFs from “ABCABC...” to “ABCABABC...”. The region of the grain sheared in presence of SFs changes the misorientations across the GB in configuration with pre-existing SFs, NPC_{SF} , as shown in Fig. 2c. The misorientation angles for the GB between grain numbers 3 and 4 are 62° and 59° at different locations of the GB and are different from the angles between the same grains in defect-free configuration NPC_0 . Therefore, the insertion of SFs in the nanograins modifies the local misorientation of the GBs, and the same applies to the other GBs in this simulation configuration.

During the martensitic transformation, various processes are observed. For clarity and better illustration, in Figs. 3, 4, and 5 we refer to these by the notations summarized in Table 2. The representative cases of martensitic transformation for each configuration with grain centers 1 are discussed in the next subsections. The same qualitative mechanisms were observed for the simulation system with grain centers 2 and with the variation of distance between the planar faults in configurations with pre-existing TBs and SFs.

Martensitic transformation in configuration NPC_0 (without pre-existing defects)

Figure 3a–f shows the evolution of the microstructure as a function of cooling for configuration without defects. The microstructures seen in Fig. 3a, b during cooling at 90 K, originate from the equilibration

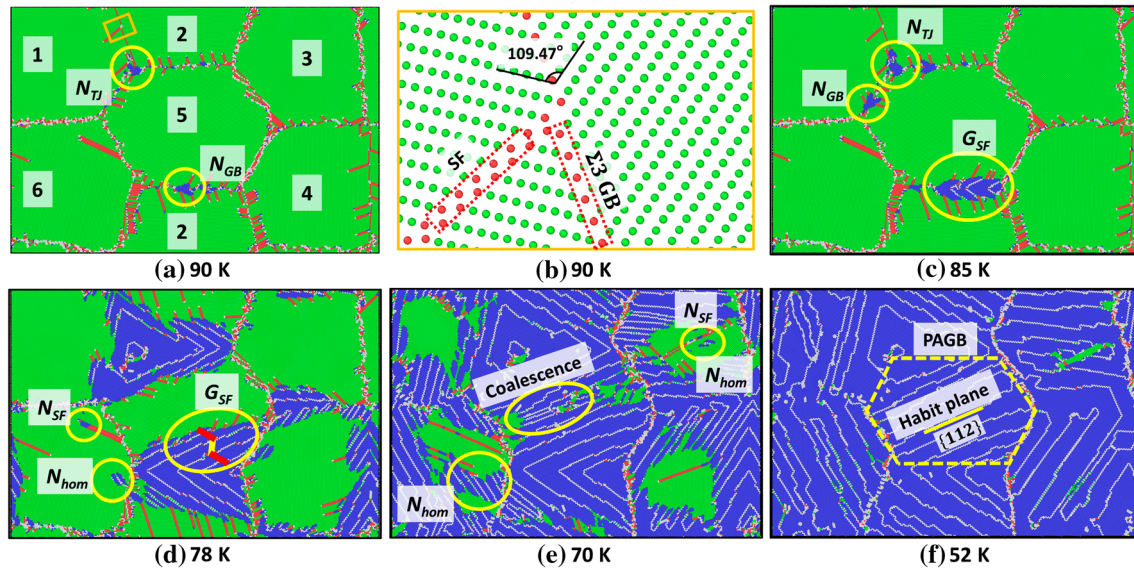


Figure 3 Microstructure evolution during cooling for configuration NPC_0 as a function of temperature. Refer to Fig. 1 and Table 2 for the interpretation of atomic colors and letters, respectively.

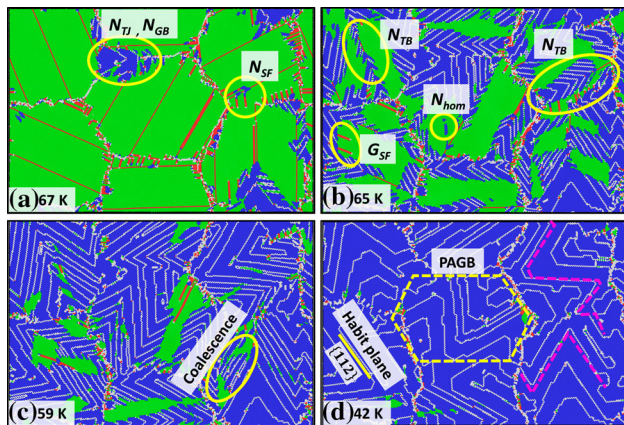


Figure 4 Microstructure evolution during cooling for configuration NPC_{TB} ($\lambda_{TB} = 80.8 \text{ \AA}$). Refer to Fig. 1 and Table 2 for the interpretation of atomic colors and letters, respectively.

process at 1200 K. Figure 3a shows the state of the simulation system after the nucleation of martensite and the structure of the GBs. The SFs nucleate from the incoherent regions of the GBs and can be seen as two layers of red atoms with hcp stacking. This is consistent with the emission of the partial dislocations at the GBs observed in different fcc metals with low SFE [36] and is explained by Ritter et al. [64]. The heterogeneous nucleation of the martensite was observed at 90 K at a triple junction (marked by the notation “ N_{TJ} ”) and at the intersection of GB (“ N_{GB} ”) in Fig. 3a.

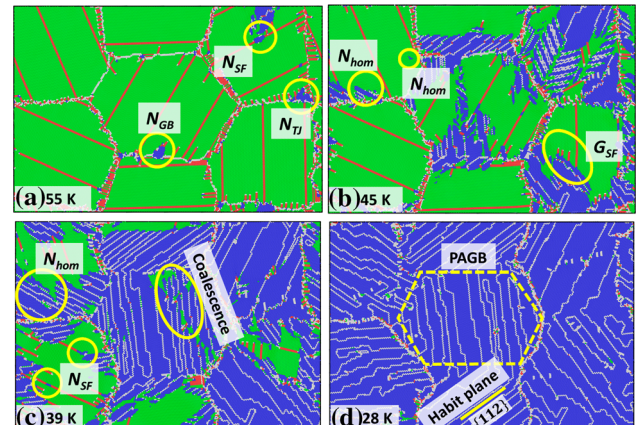


Figure 5 Microstructure evolution during cooling for configuration NPC_{SF} ($\lambda_{SF} = 78.7 \text{ \AA}$). Refer to Fig. 1 and Table 2 for the interpretation of atomic colors and letters, respectively.

During equilibration at 1200 K, the high thermal vibrations of the atoms decompose the GBs into a low energy state consisting of faceted symmetric tilt grain boundaries. The misfit is accommodated by the generation of SFs at the facets which can be observed at the closeup view of the monolayer of atoms in Fig. 3b, corresponding to the orange rectangle of Fig. 3a between grain numbers 1 and 2. The misorientation angles for the two GBs between grain numbers 1–2 and 4–6 (111.1° and 112.7° , respectively) before equilibration are closer to that of $\Sigma 3$

Table 2 Summary of the letters used to indicate the different phenomena observed during the fcc-to-bcc martensitic transformation in Figs. 3, 4 and 5

Letter	Phenomena
N_{TJ}	Martensite nucleation at grain boundary triple junction
N_{GB}	Martensite nucleation at GBs or at the intersection of GBs and SFs
N_{SF}	Martensite nucleation at SFs
G_{SF}	Martensite growth accompanied by the propagation of the SFs
N_{hom}	Homogeneous nucleation of martensite
N_{TB}	Martensite nucleation and growth at TBs

$(111)_1/(11\bar{1})_2$ $109.47^\circ/[1\bar{1}0]$ coherent symmetric tilt grain boundary in fcc austenite. Therefore, they decompose to form a special type of $\Sigma 3$ GB containing TBs along with the SFs nucleating from them, both of which are marked by dashed rectangles in this figure. The SFs nucleated at these TBs help maintain the lattice matching in the two grains. Rittner et al. [64] have described such a dissociation of GBs into low energy GB structures along with the emission of SFs from the GBs. Note that, the coherent symmetric tilt grain boundary was not pre-created along with the simulation system, random orientations were assigned to the different grains during the creation of the different configurations. The coherent symmetric tilt grain boundary is generated here during the equilibration.

With a further decrease in temperature to 85 K as shown in Fig. 3c, multiple heterogeneous nucleation sites of martensite variants are observed at the intersection of GBs and SFs. One of these sites is marked by N_{GB} . The growth of the heterogeneously nucleated martensite accompanied by SFs is indicated by G_{SF} . At 78 K, 18.98 at.% fcc have transformed to bcc as seen in Fig. 3d. The growth of the heterogeneously nucleated martensite variants is observed here. The martensite growth is accompanied by the propagation of the SFs at the fcc/bcc interface boundary as marked by G_{SF} . The martensite phase grows in lath morphology and two variants are formed across the GB in each grain, this is also marked by the notation G_{SF} and the corresponding ellipse in this figure. The formation of equivalent variants on either side of the GBs maintains the compatibility of transformation strain across the boundary. This type of nucleation has been referred

to as cooperative nucleation by Ueda et al. [65]. The red and yellow lines marked within the ellipse show the $\langle 111 \rangle_{bcc}$ directions. These directions are mirror images of each other indicating that the martensite forms in a twinned morphology. The gray atoms between the two martensite variants indicate the $\{112\}$ habit plane of the martensite. At some locations, the martensitic transformation at SFs and homogeneous nucleation are also observed as indicated by the letters N_{SF} and N_{hom} , respectively. The homogeneous nucleation is observed when the martensitic transformation has already happened in the surrounding regions or grains. The high transformation strain created by the surrounding martensite leads to homogeneous nucleation. Homogeneous nucleation was also observed in a previous simulation study [19].

Homogeneous nucleation and nucleation at SFs are observed at other regions in the simulation systems, as marked in Fig. 3e, at a decreased temperature of 70 K. The growth of the homogeneously nucleated martensite can be seen in grain 6 as marked by N_{hom} . Several martensite variants with a low lamella thickness are observed within the yellow ellipses in this subfigure. The fcc-to-bcc transition process leads to large transformation stresses and the formation of incoherent TBs in the bcc martensite. The coalescence process reduces the transformation strain within the transformed grains and thereby reducing the energy. As seen in the next Fig. 3f at 52 K, the lower thickness lamella is replaced by the larger thickness martensite variants at the same location. The transformation completes with most of the fcc austenite phase transformed to bcc martensite having lath morphology. The dashed hexagon in this subfigure indicates the prior austenite grain boundary (PAGB). The misorientation between the different martensite laths after transformation is observed as gray atoms, identified by a-CNA, in Fig. 3f. One such misorientation is indicated as the habit plane $\{112\}$ of martensite, which is the martensite TB, in this figure. The martensite variants across the habit plane or TB are oriented mirror images of each other. Such a twinned morphology of martensite is also observed experimentally in Fe alloys [66]. Note that, only in grain number 6 the growth of the homogeneously nucleated martensite is observed. In other grains, the growth of the heterogeneously nucleated martensite consumes the homogeneously nucleated martensite. The same type of transformation features are

observed for the simulation system with grain centers 2 of configuration without defects, i.e., NPC_0 .

Martensitic transformation in configuration NPC_{TB} (presence of pre-existing TBs)

Figure 4a–d shows the transformation during cooling in configuration NPC_{TB} , with pre-existing TBs, with $\lambda_{TB} = 80.8$ Å. As mentioned before, the structure of the GBs in this configuration is different compared to the defect-free configuration. Nevertheless, several features of the transformation process are common to the previous configuration. At 67 K, heterogeneous martensite nucleation is observed at triple junctions and grain boundaries, indicated by notations N_{TB} and N_{GB} , respectively, in Fig. 4a. The nucleation of SFs from the GBs is observed in this figure. The martensite nucleation is also observed at SFs and at the intersection of SFs and TBs (marked by the notation N_{SF}). At the GB location indicated by N_{SF} , the minimal mismatch between the neighboring grains is accommodated by atomic rearrangement and generation of SFs during equilibration at 1200 K. Therefore, the a-CNA algorithm identifies this local region without any GB as shown in this figure and Fig. 2b.

Figure 4b shows the nucleation and growth of the martensite variants from the TBs at several locations in the simulation system at a reduced temperature of 65 K. A couple of these locations are marked by the letter N_{TB} . At this temperature, 46.8 at.% of fcc has transformed to martensite. The two martensite variants grow from the GBs and also from TBs. The growth of the martensite from the TBs is also observed in Fe-Ni alloys experimentally [21] and is referred to as Chevron morphology. The growth of the martensite from the GBs is accompanied by the propagation of the SF (marked by G_{SF}). The high fraction of transformed martensite from the GBs and TBs induces high transformation strains in the simulation system which results in the rapid homogeneous nucleation marked by N_{hom} in Fig. 4b. The growth of martensite variants from different locations leads to their overlapping and coalescence as indicated in Fig. 4c. The transformation completes at 42 K as shown in Fig. 4d. The PAGB and the habit plane of the martensite variants are marked in this figure. The dashed pink lines indicate a zigzag morphology of the transformed martensite, and it is formed because of the presence of the pre-existing TBs in this configuration. The orientation of the transformed

martensite (as indicated by the orientation of the habit plane $\{112\}$) is different in each grain compared to the configuration without defects, and this is because of the different atomic transformation mechanisms in this system, which will be described in the discussion Sect. 4.

Thus pre-existing TBs affect the nucleation, growth, morphology, and orientation of the martensite formation. The same transformation features are also observed for the different spacing of the TBs and the simulation system with grain centers 2. The decrease in spacing of TBs or increase in the number of TBs in the austenite grains produces transformed martensite with a highly zigzag morphology. This happens because each TB leads to a change in the orientation of the boundary between the transformed martensite variants, leading to increased zigzag nature, see figure S1 in the supporting information for $\lambda_{TB} = 27.6$ Å with grain centers 2. Also, a greater number of TBs at reduced spacing provide additional heterogeneous nucleation sites, thereby reducing the homogeneous nucleation in the nanograins. This results in the formation of numerous smaller-sized martensite lamella, which leads to a qualitatively increased coalescence rate of the incoherent martensite TBs. The quantitative measurement of the coalescence rate of martensite variants is beyond the scope of this work.

Martensitic transformation in configuration NPC_{SF} (presence of pre-existing SFs)

The transformation process for the configuration with pre-existing SFs with $\lambda_{SF} = 78.7$ Å is shown in Fig. 5a–d. At 55 K, in figure 5(a), the nucleation of martensite at GBs (N_{GB}), triple junctions (N_{TJ}), and at the SFs (N_{SF}) is observed. The decrease in the temperature to 45 K exhibits the other features of the transformation process i.e., growth accompanied by SFs (G_{SF}) and homogeneous nucleation (N_{hom}) as shown in Fig. 5b. Here, 23.7 at.% of the fcc has transformed to bcc. The combined effect of the stress state of the pre-existing SFs, newly nucleated SFs from the GBs, and the thermally induced stresses in the simulation system causes homogeneous nucleation and growth at several places in the simulation system. As before, homogeneous nucleation is observed only when the transformation has already happened in the surrounding region of the grain or neighboring grains in the simulation system.

At 39 K, Fig. 5c, the growth of the martensite variants from opposite GBs leads to coalescence. The 58.6 at.% transformation has been completed at this stage. The homogeneously nucleated martensite variants grow only in grain number 1, as indicated by N_{hom} . In other grains, the growth of the heterogeneously nucleated martensite consumes the homogeneously grown martensite. The transformation completes at 28 K as shown in Fig. 5d. The dashed hexagon indicates the PAGB and the yellow line indicates the habit plane of martensite. The same type of transformation mechanisms were observed for configuration with pre-existing SFs with the decrease in SF spacing, and the simulation systems with grain centers 2. However, the decrease in SF spacing increases the number of heterogeneous sites available for the martensite nucleation and growth, and also increases the internal stresses in the grains. This results in mostly heterogeneous nucleation and growth while suppressing the homogeneous nucleation of the martensite, see figure S2 in supplementary material.

From Figs. 3f, 4d, and 5d, it can be seen that the orientations of the martensite laths in each grains of these configurations are different after the transformation is complete. The introduction of the nanospaced TBs and SFs changes the atomic structure of the GBs, which leads to different transformation mechanisms and different orientations of the martensite laths in each configuration after the transformation, which will be discussed in the next section.

Discussion

The evolution of the fraction of bcc structure during cooling is shown for configuration with pre-existing TBs (Fig. 6a) and configuration with pre-existing SFs (Fig. 6b). In both figures, the data for the configuration without defects is also shown as $\lambda^{-1} = 0$. It is observed that the transformation proceeds rapidly after transformation to 2 at.% bcc phase for all the configurations. Therefore, the temperature at this

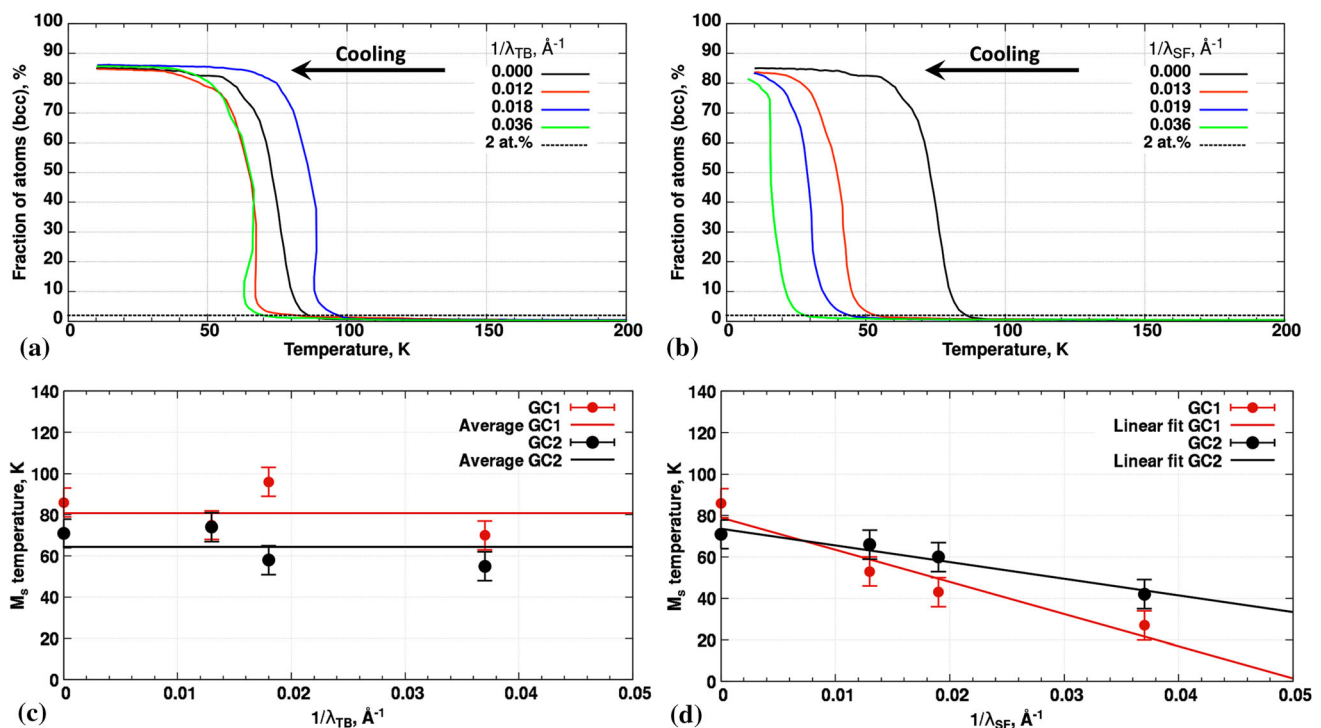


Figure 6 The evolution of fraction of atoms with bcc structure during cooling in different configurations with grain centers 1, marked as inverse of their defect spacing ($1/\lambda$), for **a** configurations NPC_0 and NPC_{TB} , and **b** configurations NPC_0 and NPC_{SF} . The M_s temperature as a function of inverse of defect

spacing for **c** configurations NPC_{TB} containing pre-existing TBs, **d** configurations NPC_{SF} containing pre-existing SFs. $\lambda^{-1} = 0$ indicates configuration NPC_0 . Abbreviations GC1 and GC2 represent configurations with grain centers 1 and 2, respectively.

value (indicated by the dashed line) is considered as the martensite start temperature (M_s). In the next subsection, we discuss the effect of defect spacing on the M_s temperature.

Effect of defect spacing on the M_s temperature

The M_s temperature can be determined by analyzing the evolution of different properties, e.g., density, volume, and/or potential energy. The density data for the simulation configurations with grain centers 1 are presented in supplementary figure S3. It can be seen that the density follows the same trend as the fraction of atoms, and the calculation of M_s temperature using the density data (2% deviation from the observed density trend during cooling of the austenite phase) gives the same result as that obtained from the analysis of the fraction of atoms. So, the analysis of the fraction of atoms is used in the present work to correlate the microstructure development and to demonstrate the effect of planar defects on the mechanisms. The density at 200 K is 7.4 g/cm³ from MD simulations, which shows only a 5% deviation from the experimentally obtained density [67].

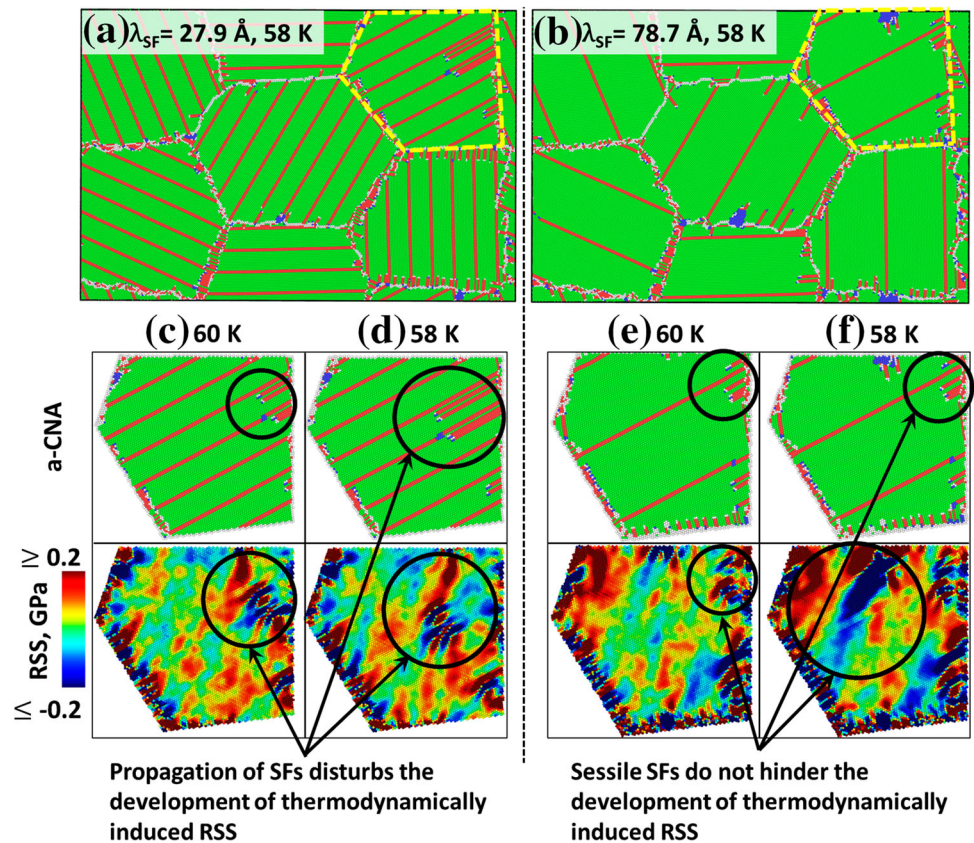
The M_s temperature as a function of inverse of defect spacing (i.e., λ^{-1}) for different configurations is shown in Fig. 6c, d. The $\lambda^{-1} = 0$ indicates the configuration without defects. The data for grain centers 1 (GC1) and grain centers 2 (GC2) is included here. The error bars indicate the variation of M_s temperature for the same configurations with different initial velocities of the fcc phase at 1200 K. The M_s temperature for nano-polycrystalline systems with pre-existing TBs does not show a clear trend (see Fig. 6c). On the other hand, the M_s decreases linearly with the decrease in the SFs spacing as seen in Fig. 6d. This peculiar behavior in presence of pre-existing TBs or SFs is a consequence of different effects such as the state of the GBs after equilibration, atomic displacements leading to martensitic transformation, and resolved shear stresses on the slip system.

The M_s temperature for Fe in the present simulations is significantly lower (from 40 to 100 K depending on pre-existing defects) than observed in experiments and theoretical predictions. The selected Meyer–Entel EAM formalism for Fe has been extensively demonstrated [19, 20, 46, 47, 53] to be useful

and capable of showing fcc-to-bcc transformation during cooling from the austenite phase, but it is an inherent limitation of this interatomic potential that the M_s temperature deviates from the observed experimental data. However, it is still considered the most adequate for the present work, which is to study the progress of martensite formation in the presence of planar faults. Additionally, the nanograin system size in this work differs significantly from the typical grain sizes achieved in experimental polycrystalline Fe samples. As discussed in the introduction, nanocrystalline-sized austenite can delay M_s to very low temperatures or completely suppress the martensitic transformation, which is in agreement with the current observations. For single-crystal Fe simulation systems with periodic boundary conditions (infinite length of the single grain along all directions) using the same Meyer–Entel interatomic potential, previous simulation studies showed that the M_s temperature: (i) varies from 150 to 400 K based on the analysis of atomic volumes [20, 53], and (ii) is around 550 K from the calculation of free energies [46]. This M_s value for single crystal systems is much higher than the one observed in the present work with nano-polycrystalline grains. Therefore, we can also hypothesize that the deviation could be a result of the nanometer austenite grain sizes and the presence of planar defects used in this work. Although the M_s temperature in this work differs from observed experimental data, considering the influence of the interatomic potential influence, the results are interpreted in relative terms, i.e., M_s changes correctly with varying microstructure features of planar defects. Therefore, we focus on the facts that: (i) the correct transformation mechanisms are reproduced in presence of pre-existing planar defects, and (ii) qualitatively correct trends of change in M_s temperature as a function of the distance between the planar defects could be observed and proposed in this work. The simulations and corresponding results are able to achieve both of these aims.

The M_s temperature represents the start temperature for the change in the crystal structure from fcc-to-bcc. To understand the effect of pre-existing nano-spaced planar defects on M_s temperature, it is important to know how they affect the initial nucleation and growth of the martensite. To analyze this, we calculate the atomically resolved shear stresses (RSS) in the presence of different spacing of SFs (i.e.,

Figure 7 The resolved shear stresses in presence of different spacing of the SFs in configuration NPC_{SF} grain centers 1. The top and middle rows are color coded by a-CNA, whereas the bottom row shows the atomic resolved shear stresses as per the color bar.



$\lambda_{SF} = 27.9$ and 78.7 \AA) in grain 3 of configuration with pre-existing SFs. The six components of the stress tensor were resolved on the slip system on which the atomic shears were observed in this grain to calculate atomic RSS. The RSS were calculated before the nucleation of martensite takes place in the grain. The thermally induced RSS control the atomic shear that lead to fcc-to-bcc martensitic transformation during cooling. A clear development of RSS before martensite nucleation will indicate that the atoms will move along a particular slip system, which will induce the transformation. A disturbed pattern or irregular development of RSS will indicate that atoms will not shear along a particular slip system.

Figure 7a, b shows the configuration with pre-existing SFs for two different λ_{SF} . The close-up view of the yellow-dashed grain number 3 is shown in the bottom two rows. The characterization by a-CNA and RSS is shown at 60 and 58 K, respectively, before nucleation of martensite. The bcc martensite seen at 58 K for $\lambda_{SF} = 78.7 \text{ \AA}$ does not grow until a further decrease in temperature to 50 K. At 60 K, in addition to the pre-existing SFs which go from one GB to another GB within the grain, new SFs can be seen

nucleating from the GBs in both the configurations as marked by the black circles in Fig. 7c, e. The propagation of the leading partials of these new SFs can be seen parallel to the pre-existing ones. At this stage, three types of stress states interact with each other in the grain: pre-existing SFs, newly generated SFs from the GBs, and thermally induced stresses. The corresponding atomic RSS is shown in the bottom row of this figure. At 60 K, higher magnitudes of the RSS can be seen for $\lambda_{SF} = 27.9 \text{ \AA}$ than in $\lambda_{SF} = 78.7 \text{ \AA}$. The higher RSS induce the propagation of the leading partial of newly nucleated SFs (parallel to the pre-existing SFs) at 58 K for $\lambda_{SF} = 27.9 \text{ \AA}$ system (see Fig. 7d). The propagation of SFs, in turn, resists the development of thermally induced RSS which can induce the atomic shear leading to the fcc-to-bcc transformation. This disturbs the development of the RSS in this grain and the irregular arrangement of the RSS can be seen here (see bottom row of Fig. 7d).

For $\lambda_{SF} = 78.7 \text{ \AA}$, lower magnitude of RSS are observed at 60 K compared to the $\lambda_{SF} = 27.9 \text{ \AA}$ system (see bottom row of Fig. 7c, e marked by black circles). The leading partials of the SFs do not propagate and stay at the same location at 58 K (see

Fig. 7e, f). The immobile SFs do not induce RSS and do not create a hindrance to the thermally induced RSS. Therefore, a clear development of the RSS, with high positive and negative magnitudes can be seen in Fig. 7f marked by a black circle. These high atomic RSS lead to the atomic shear causing the martensitic transformation.

Thus, it is observed that the decrease in distance of SFs causes the propagation of the new SFs from the GBs which hinders the build-up of the thermally induced RSS in the grain, and thereby hinders the martensitic transformation and reduces the M_s temperature. The RSS for the configurations with and without TBs were also investigated (see figure S4 in the supporting information) showing the clear development of the atomic RSS without any hindrance caused by the nucleation of the new SFs from the GBs in this system. In addition, the TBs dominate the transformation in the corresponding configuration by providing heterogeneous nucleation and growth sites. The variation of the nucleation and M_s temperature, in this case, are statistical in nature generated by the random initial velocities used to equilibrate the austenite samples at a higher temperature, hence the absence of a clear M_s trend and the observance of small differences in the temperatures at which nucleation begins. Therefore, in

Fig. 6c, the M_s temperature for TB 55 Å (i.e., $1/\lambda_{TB} = 0.018 \text{ Å}^{-1}$) configuration with grain centers 1 is higher than observed in the defect-free configuration (i.e., $1/\lambda_{TB} = 0 \text{ Å}^{-1}$), while the opposite trend is observed when the configurations with grain centers 2 are considered.

Atomistic transformation mechanisms

Pre-existing defects also affect the atomic pathways during the transformation. These pathways are summarized in Fig. 8a–d at four locations depending on the slip systems involved during the transformation, and the orientation relationships between the parent and product phases. At least two or more of these categories were observed in each of the configurations studied in this work depending on the local arrangement of the atomic planes. In this figure, one atom thick layers (or monolayers) at different locations are chosen to focus on the atomic shears during the transformation. The arrows at the head of the atoms indicate the atomic displacements calculated with respect to the previous configuration (1 ps difference) and are scaled by 2.5 for better visualization. The red arrows indicate the general direction of the group of atoms. The side view is shown in all

Figure 8 Atomic displacements leading to the martensitic transformation at different regions in the three configurations studied. The atoms are color coded by a-CNA.

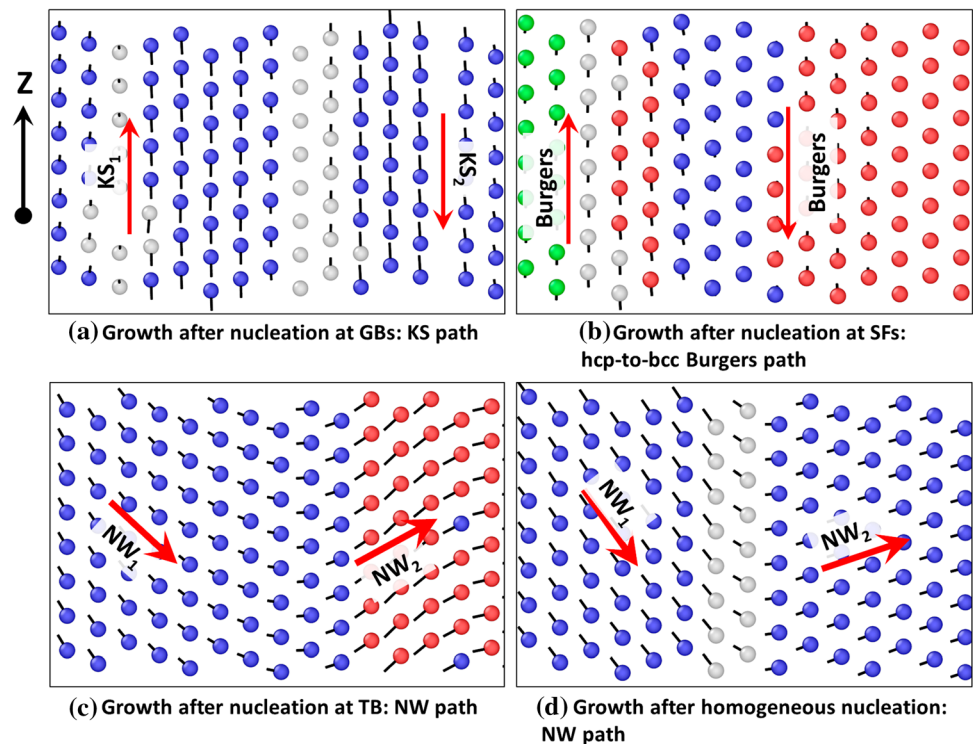
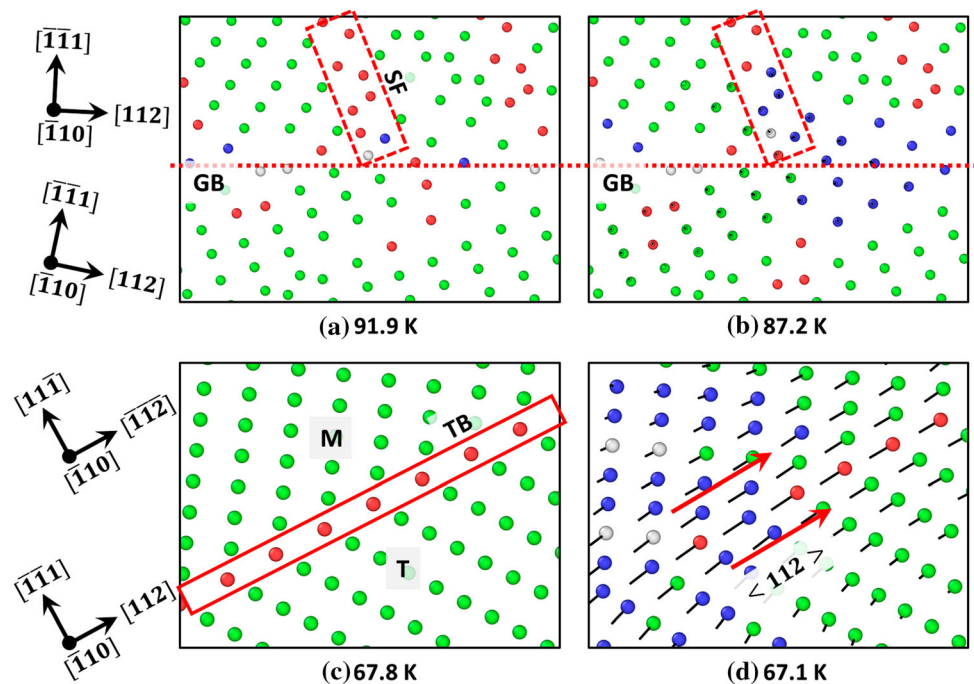


Figure 9 The atomic mechanisms that lead to the **a, b** K–S transformation at GBs. The horizontal dashed line indicates the GB and the dashed rectangle indicates two layers of SF. **c, d** N–W transformation mechanism in presence of TBs. The solid rectangle indicates TB (monolayer of atoms in hcp stacking). M = matrix orientation, T = twinned orientation. The atoms are color coded by a-CNA.



the sub-figures with the Z-axis pointing vertically upwards as marked in the figure.

Figure 8a shows the atomic displacements at and close to one of the intersections of GB and SF that lead to the heterogeneous nucleation and growth of the martensite. This slice is taken from the configuration NPC_0 , without defects, in Fig. 3c at the area marked by an ellipse and G_{SF} in grain number 5. The atomic shears observed here are vertically upwards and downwards along the Z-axis of the simulation system, respectively i.e., $\{111\} \langle 1\bar{1}0 \rangle_{fcc} \parallel \{110\} \langle 111 \rangle_{bcc}$ slip systems. This orientation relationship indicates the K–S path. The atomic shears of groups of atoms along the two opposite directions produce the two K–S variants of martensite from GBs, which reduces the misfit strains produced in the grain during the transformation process. The gray atoms between the two K–S variants form TB between the transformed martensite variants. Although the atomic mechanism is shown for the monolayer from configuration without defects, the same type of atomic shear was observed in other configurations with pre-existing SFs when there is nucleation and growth of martensite at the intersection of GBs and SF, and triple junctions.

The growth after nucleation at the SFs happens by the hcp-to-bcc Burgers path [68] as seen in Fig. 8b. The atoms at the SFs displace on the

$\{0001\} \langle 11\bar{2}0 \rangle_{hcp}$ slip system, and transform to $\{110\} \langle 111 \rangle_{bcc}$ slip system. The red arrows indicate the atomic shear along $\langle 11\bar{2}0 \rangle_{hcp}$ directions. This monolayer of atoms is analyzed for configuration with pre-existing SFs (see Fig. 5a), but the same mechanism is valid whenever there is local transformation at the SFs.

The transformation at the atomic layer of TBs and the homogeneous nucleation within the fcc phase happens by the N–W transformation path [11], as seen in Fig. 8c–d, respectively. The two N–W variants produced by these atomic displacements are along $\{111\} \langle 112 \rangle_{fcc} \parallel \{110\} \langle 110 \rangle_{bcc}$ slip systems. The alternating pattern of the N–W variants generates a twinned morphology of martensite and also reduces the transformation strain in that grain. In Fig. 8c, the left part has already been transformed, whereas the right half part is in the process of the transformation. The right part will transform with a decrease in temperature. After transformation, the atoms between the two variants N–W₁ and N–W₂ will become martensite TB and will be identified as gray by a-CNA. The monolayer of TB and homogeneous nucleation is taken from the configuration with pre-existing TBs (see Fig. 4b area marked as N_{TB} in grain 1) and the configuration with pre-existing SFs (Fig. 5b area marked as N_{hom} in grain 1), respectively. The same type of atomic displacements were observed in

other configurations when homogeneous nucleation and growth of martensite or transformation at TB happens.

The presented atomistic pathways were observed in many experimental [65, 69, 70] and simulation studies [19, 63] but none has explained the probable cause for the preferential existence of K–S vs N–W mechanism at different locations such as GBs, TBs, and SFs. To understand why the K–S mechanism was observed for the heterogeneous martensite nucleation and growth at the intersection of GBs and SFs, a closer look at the monolayers is taken in Fig. 9a, b. The coordinate axes show the corresponding fcc directions for the two grains across the GB (indicated by the red dashed line). The rectangle indicates the atoms at the SF which nucleate from the GB as seen in Fig. 9a. At a reduced temperature of 87.2 K (Fig. 9b) the atoms of the SF shear by hcp-to-bcc Burgers mechanisms, which is represented by $\{0001\} \langle 11\bar{2}0 \rangle_{\text{hcp}} \parallel \{110\} \langle 111 \rangle_{\text{bcc}}$. The atomic shear directions are perpendicular to the plane of the paper, and therefore not visible clearly in this figure. However, they can be visualized in the previous Fig. 8b projected in the side view. Once the atomic shear has been initiated by the Burgers mechanism, the surrounding atoms in the grain (with fcc structure) also shear so that they follow the $\{110\} \langle 111 \rangle_{\text{bcc}}$ slip system, which reduces the misfit between the transformed martensite at the neighboring locations i.e., at the SFs and the fcc region surrounding SFs. This essentially leads to a $\{110\} \langle 111 \rangle_{\text{bcc}} \parallel \{111\} \langle \bar{1}10 \rangle_{\text{fcc}}$ K–S transformation pathway. Therefore, the nucleation of new SFs at the GBs leads to a two-step transformation process - first the Burgers path at the SFs which is followed by the K–S path in the surrounding fcc matrix.

To understand why the transformation at TBs follows the N–W mechanism, a closer view of the atomic arrangements of the TBs is shown in Fig. 9c, d in configuration with pre-existing TBs and grain number 3. The TB is indicated by a red rectangle and consists of a single layer of red atoms. The coordinate axes show the orientation of the matrix and twinned regions across the TB. The original orientation is marked as “M” (matrix) and the mirror image region is marked as twinned “T.” Across the TB plane, $[\bar{1}10]_{\text{fcc}}$ the direction is the same for matrix and twinned regions, and the other two directions are mirror images of each other. During the

transformation, the common direction remains an invariant line, and the atomic shear proceeds along the two $\langle 112 \rangle_{\text{fcc}}$ directions across the TB. This keeps the misfit strains to a low value, and the $\langle 112 \rangle_{\text{fcc}}$ direction of the TB changes to $\langle 110 \rangle_{\text{bcc}}$ direction. Although the analysis explained here for the TBs in a columnar or preferentially oriented system, it should be valid for a system with randomly oriented grains as the local arrangement across the TB in the fcc phase is the same in both these systems.

The homogeneous nucleation is observed only when the substantial fraction (at least 25 at.% or more) of fcc has transformed to bcc in the surrounding regions or grains. The transformation in the nearby regions creates the atomic RSS on the N–W slip system. The build-up of the atomic RSS is shown for the configuration NPC_0 , without defects, grain 6 in the supporting information figure S5(a–c). The RSS on the N–W and K–S slip systems in this grain as a function of the decrease in the temperature before the martensite nucleation are compared. It can be seen that the RSS on the N–W slip system is higher than the K–S slip system at 82 K, and therefore the transformation happens by the N–W mechanism.

The K–S and N–W transformation mechanisms have been observed in several studies [19, 63, 69], but the conditions why a particular mechanism is observed are not discussed. They also do not analyze the atomistic displacements during the transformation, instead, analyze the pictures after the transformation has been completed. Meiser and Urbassek used a bicrystalline simulation system with $[100]_{\text{fcc}}$ tilt axis [71], with different CSL boundaries, in fcc austenite to understand the transformation mechanism. They observed the K–S transformation mechanism in this system, indicating the role of GBs and possibly the SFs in transformation as per the K–S pathway. Song and Hoyt [63] used nano-polycrystalline fcc system with $\langle 110 \rangle_{\text{fcc}}$ tilt axis. They observed the nucleation of TBs and SFs from the GBs, as in the present work. The transformation followed the K–S and N–W transformation pathways, with the K–S being the dominant mechanism in all ferrite grains due to its low interfacial energy. We also observed that the K–S transformation pathway is dominant in most of the grains, but we present here the reasoning based on crystallography rather than energetics. Additionally, our analysis provides insights into the presence of N–W transformation mechanisms at TB

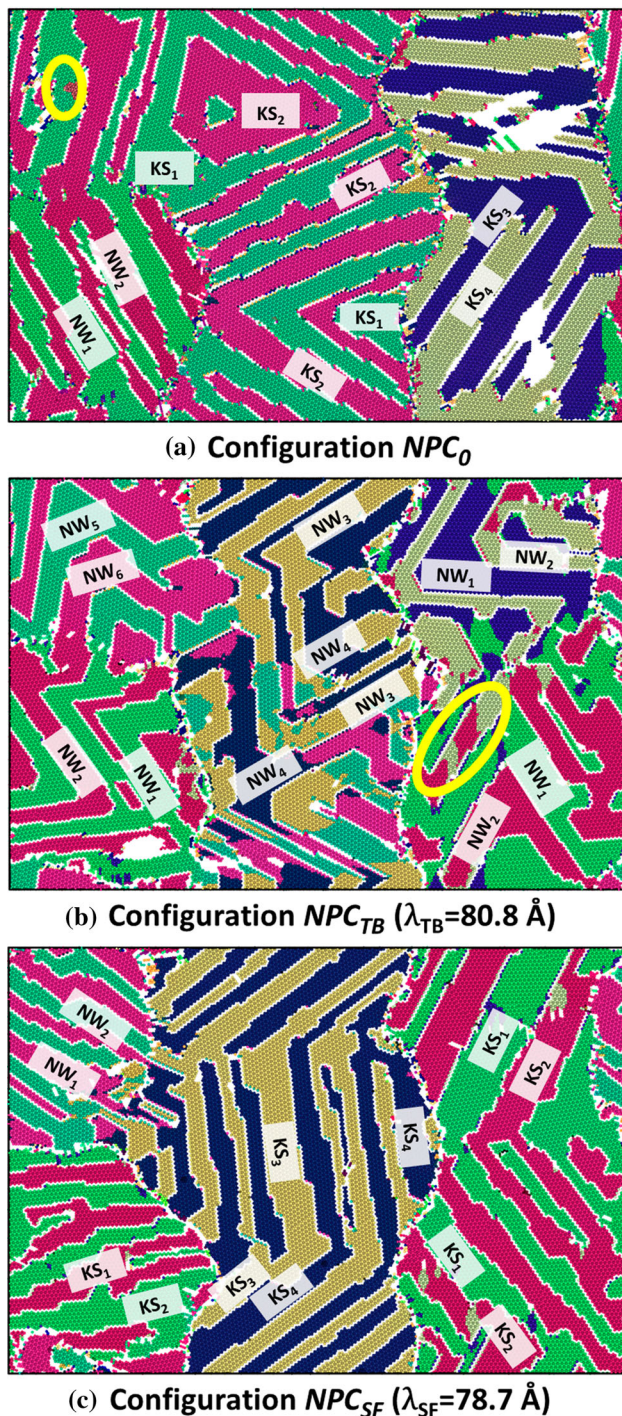


Figure 10 The orientations of martensite variants after transformation in different configurations. The atomic colors indicate orientations as projected into Rodrigues–Frank space. The different variants are also marked as per the slip systems followed during the transformation in Fig. 8.

and for homogeneous nucleation. In a Fe–30 at.%Pd alloy, Tanaka and Oshima [72] observed the N–W transformation path in presence of austenite twins.

This observation supports our conclusion that martensitic transformation follows the N–W path in presence of austenite TBs.

Martensite variants

The orientations of martensite variants were calculated and subsequently projected into the Rodrigues–Frank space to clearly visualize the different orientations of martensite variants, following the method described in [44]. The colors in Fig. 10a–c indicate different orientations or variants of martensite as per the Rodrigues–Frank values converted to the RGB color scale. These orientations are correlated with the atomistic displacements described in Fig. 8 and “Atomistic transformation mechanisms” section and are marked on each of the laths of martensite. Similar colors indicate similar martensite orientations and variants. It is worth mentioning that close to the boundaries of fundamental zones, two atoms with very similar orientations can have large misorientations. This situation is identified at a couple of locations, marked with a yellow ellipse in Fig. 10a–b. There is a minimal orientation difference between the N–W and K–S variants marked in these figures because these two variants differ by only 5.26° . The exact orientation relationships for these variants are given in the supporting information table T1, which were calculated by analyzing the slip planes and directions.

In configuration without defects and with pre-existing SFs (seen in Fig. 10a, c, both K–S and N–W variants are observed. The martensite nucleated heterogeneously from the intersection of GBs and SFs form K–S variants and the homogeneous nucleation leads to N–W variants. In both these configurations, the K–S mechanism dominates the transformation, with five of the six grains following this mechanism. Only one grain in these configurations transforms by the N–W mechanism. However, the configuration with pre-existing TBs show only N–W variants (see Fig. 10b), indicating the dominance of the N–W pathway of transformation.

General remarks

As mentioned in Sect. 2, the results for configuration without defects using MEAM potential are shown in supplementary material figures S6. Several key features of the transformation process are observed

using this potential as well. The orientation and the type of martensite variants after the transformation are the same as Meyer–Entel EAM potential. The same qualitative results are observed for configurations with pre-existing TBs and SFs using MEAM potential, as for the Meyer–Entel EAM potential. This indicates that the mechanisms presented reflect the effects of planar defects and are not significantly affected by a different interatomic potential.

In this work, pure Fe with preferentially oriented nano-polycrystalline simulation systems, with a $\langle 110 \rangle_{\text{fcc}}$ tilt axis, are used. The real samples consist of random GB misorientations and alloying elements. Both of these factors might lead to the existence of other mechanisms such as Pitsch [73] or Greninger-Troiano [74]. Therefore, the mechanisms proposed here apply to the simulation system with $\langle 110 \rangle_{\text{fcc}}$ tilt axis described here. Nonetheless, the analysis elucidated in this work helps to understand the transformation mechanisms and could be applied to simulation systems with randomly oriented grains or alloying systems in future studies.

To make sure that the length of the periodic direction Z does not affect the martensitic transformation, a larger Z dimension length of 6.25 nm for the defect-free configuration was simulated. The fraction of atoms, the density of the simulation system, and the evolution of microstructure during cooling are shown in supplementary figure S7(a–c), and the different microstructural features of transition are also marked. The mechanisms of phase transformation and the magnitude of M_s temperature do not change with an increase in Z dimension length. The initial nucleation of the bcc phase starts at 98 K and the rapid transformation happens after the transition to 2 at.% fraction of bcc structure. The corresponding M_s temperature, in this case is 95 K. This value is comparable to the system with a smaller Z dimension of 2.09 nm where M_s is 87 ± 7 K (the variation is the result of the simulations with different initial velocities used to equilibrate the austenite phase at 1200 K). The number of martensite twins formed in each grain varies from 7 to 9 and is the same in smaller and larger simulation systems. Homogeneous nucleation is observed in only one grain when approximately 30 at.% transformation has been completed from the heterogeneous nucleation and growth in the surrounding grains or region within the same grain. Similar to the smaller systems,

homogeneously nucleated martensite is not stable and is consumed by the growth of the martensite lamella nucleated heterogeneously at GBs or triple junctions during cooling. At the nanocrystalline grain sizes, such as used in this work, high transformation strain is generated during transformation which provides enough energy for homogeneous nucleation. In a much larger simulation cell, e.g., also increasing dimensions along X–Y directions, heterogeneous nucleation and growth would not generate such high transformation strains, and therefore, it is expected that either the same or lower fraction of grains would display homogeneous nucleation.

Recently, lots of focus has been given to the role played by the nanoscale features such as SFs and TBs on the mechanical properties of alloys [75, 76]. The advances in characterization techniques allow for studying such nanoscale effects. However, the role played by these planar defects on the phase transformation has not been explored thoroughly in the literature yet. Fukino and Tsurekawa [3] showed that these planar faults are formed during the heating from room temperature bcc ferrite to high temperature fcc austenite phase, and their formation depends on the alloying composition and the thermomechanical treatment carried out. The presence of planar faults in the high-temperature austenite phase entails a thorough analysis of their effect on the martensitic transformation, as done in this work. As per the author's knowledge, this is the first study thoroughly analyzing the effects of nano-spaced planar defects on the martensitic transformation. Many experimental, theoretical, and simulation studies have linked the presence of planar defects with specific martensitic transformation mechanisms [3, 19, 20, 63, 70]. However, none of these explored the correlation between the distance of nanospaced defects and their effect on the atomic displacements, which subsequently leads to a particular transformation mechanism. Here we have successfully demonstrated this by an extensive analysis of the atomistic configurations.

Dislocations play an important role in the martensitic transformation, although in the present study we investigated pre-existing TBs and SFs that span the entire grain, i.e., they go from one GB to another of the same grain. For fcc crystal structures with low SFE such as Fe used in this work, the full dislocations will dissociate into partial dislocations. The

nucleation of partial dislocations can be seen from the GBs in Figs. 3a–d, 4a, b, and 5a–c. They can be observed as two layers of red atoms with hcp stacking sequence — these partial dislocations act as additional heterogeneous martensite nucleation sites marked by N_{SF} in these figures. Their effect on the transformation is discussed in detail in Sect. 4.2 and the corresponding Figs. 8b and 9a, b, specifically illustrating how these partial dislocations lead to Burgers and K–S transformation pathways of the martensitic transformation.

Conclusions

In conclusion, molecular dynamics simulations were performed to understand the role of pre-existing nano-spaced planar defects in the fcc austenite phase, i.e., twin boundaries and stacking faults, on the austenite-to-martensite phase transformation in pure Fe. Three simulation configurations were investigated: a defect-free configuration, a configuration with nano-spaced stacking faults, and a configuration with nano-spaced twin boundaries. Several features are observed during transformation in all configurations, which include: (i) stacking fault emission from the grain boundaries during equilibration of the simulation systems, (ii) heterogeneous bcc phase nucleation and growth at triple junctions, and at the intersection of stacking faults and grain boundaries. The transformation follows a two-step mechanism - hcp-to-bcc Burgers path initiated at stacking faults, which is followed by the Kurdjumov–Sachs (K–S) pathway in the surrounding fcc region of the stacking faults, (iii) homogeneous nucleation of martensite according to the Nishiyama–Wassermann (N–W) pathway, (iv) transformation at stacking faults by hcp-to-bcc Burgers path, and (v) coalescence of different martensite laths.

The analysis of the simulation results suggests a necessity to consider the role of planar defects in the martensitic transformation mechanisms by highlighting numerous observations:

- For the defect-free configurations, the transformation takes place by K–S or N–W path, depending on the nucleation and growth sites in the fcc austenite matrix. This leads to lath martensite morphology.
- In the faulted configurations, the type of planar defect, their spacing, and their orientation affect the atomic shear involved in the formation of martensite and the resulting morphology of the martensite laths.
- The pre-existing twin boundaries act as martensite nucleation sites and growth pathways. The transformation in all nanograins follows the N–W pathway and martensite forms in a zigzag morphology because of the presence of nano-spaced twin boundaries. The orientations and the distance between the twin boundaries do not show a clear effect on the martensite start temperature.
- The decrease in the spacing of pre-existing stacking faults creates additional stresses which hinder the build-up of the thermally induced shear stresses and the atomic shear leading to the transformation. Therefore, the martensite start temperature decreases with a decrease in the spacing of the stacking faults. The atomic displacements follow either N–W or K–S pathways depending on the nucleation and growth locations inside the austenite grains in presence of nano-spaced stacking faults.

Acknowledgements

The research leading to these results has received funding from the European Research Council under the European Union's Seventh Framework Program (FP/2007-2013)/ERC Grant Agreement no. [306292]. The authors would like to thank the anonymous reviewers for providing thorough comments which helped to improve the overall clarity and presentation of the manuscript.

Data availability

The input files and analysis scripts are available on request from the corresponding authors [SK and JH].

Declarations

Conflict of interest The authors declare that they have no conflict of interest

Supplementary Information: The online version contains supplementary material available at <http://doi.org/10.1007/s10853-022-07668-w>.

Open Access This article is licensed under a Creative Commons Attribution 4.0 International License, which permits use, sharing, adaptation, distribution and reproduction in any medium or format, as long as you give appropriate credit to the original author(s) and the source, provide a link to the Creative Commons licence, and indicate if changes were made. The images or other third party material in this article are included in the article's Creative Commons licence, unless indicated otherwise in a credit line to the material. If material is not included in the article's Creative Commons licence and your intended use is not permitted by statutory regulation or exceeds the permitted use, you will need to obtain permission directly from the copyright holder. To view a copy of this licence, visit <http://creativecommons.org/licenses/by/4.0/>.

References

- [1] Sarma VS, Wang J, Jian WW, Kauffmann A, Conrad H, Freudenberger J, Zhu YT (2010) Role of stacking fault energy in strengthening due to cryo-deformation of FCC metals. *Mater Sci Eng A* 527(29–30):7624–7630
- [2] Tian Y, Gorbato OV, Borgenstam A, Ruban AV, Hedström P (2017) Deformation microstructure and deformation-induced martensite in austenitic Fe–Cr–Ni alloys depending on stacking fault energy. *Metall Mater Trans A* 48(1):1–7
- [3] Fukino T, Tsurekawa S (2008) In-situ SEM/EBSD observation of α/γ phase transformation in Fe–Ni Alloy. *Mater Trans* 49(12):2770–2775
- [4] Wang HT, Tao NR, Lu K (2012) Strengthening an austenitic Fe–Mn steel using nanotwinned austenitic grains. *Acta Mater* 60(9):4027–4040
- [5] Lu K, Yan FK, Wang HT, Tao NR (2012) Strengthening austenitic steels by using nanotwinned austenitic grains. *Scr Mater* 66(11):878–883
- [6] Calcagnotto M, Ponge D, Demir E, Raabe D (2010) Orientation gradients and geometrically necessary dislocations in ultrafine grained dual-phase steels studied by 2D and 3D EBSD. *Mater Sci Eng A* 527(10):2738–2746
- [7] Shirdel M, Mirzadeh H, Parsa MH (2015) Nano/ultrafine grained austenitic stainless steel through the formation and reversion of deformation-induced martensite: Mechanisms, microstructures, mechanical properties, and TRIP effect. *Mater Charact* 103:150–161
- [8] Fine ME, Meshii M, Wayman CM, Nishiyama Z (eds) (1978) Martensitic transformation. Academic Press, Cambridge
- [9] Bhadeshia HKDH, Honeycombe RWK (2017) Steels: microstructure and properties. Fourth Edition, Butterworth-Heinemann, pp 135–177.
- [10] Kurdjumow G, Sachs G (1930) Über den Mechanismus der Stahlhärtung. *Z Phys* 64(5–6):325–343
- [11] Nishiyama Z (1934) X-ray investigation of the mechanism of the transformation from face centered cubic lattice to body centered cubic. *Sci Rep Tohoku Univ* 23:637
- [12] Olson GB, Cohen M (1972) A mechanism for the strain-induced nucleation of martensitic transformations. *J Less-Common Met* 28(1):107–118
- [13] Bogers AJ, Burgers WG (1964) Partial dislocations on the 110 planes in the BCC lattice and the transition of the FCC into the BCC lattice. *Acta Metall* 12(2):255–261
- [14] Bhadeshia HKDH, Wayman CM (2014) 9—phase transformations: nondiffusive. In: Laughlin DE, Hono K (eds) Physical metallurgy, Fifth. Elsevier, Oxford, pp 1021–1072
- [15] Kaufman L, Cohen M (1958) Thermodynamics and kinetics of martensitic transformations. *Prog Met Phys* 7:165–246
- [16] Roitburd AL (1990) On the thermodynamics of martensite nucleation. *Mater Sci Eng A* 127(2):229–238
- [17] Zhao XQ, Han YF (1999) Kinetics of homogeneous martensitic nucleation in iron-based alloys. *Metall Mater Trans A* 30(3):884–887
- [18] Qin W, Chen ZH, Zhuang YH, Du YW (2002) Possibility of the martensitic transformation triggered by thermal fluctuation. *J Alloys Compd* 340(1):114–117
- [19] Wang B, Urbassek HM (2013) Phase transitions in an Fe system containing a bcc/fcc phase boundary: an atomistic study. *Phys Rev B* 87:104108
- [20] Karewar S, Sietsma J, Santofimia MJ (2018) Effect of pre-existing defects in the parent fcc phase on atomistic mechanisms during the martensitic transformation in pure Fe: a molecular dynamics study. *Acta Mater* 142:71–81
- [21] Baur AP, Cayron C, Logé RE (2019) On the chevron morphology of surface martensite. *Acta Mater* 179:247–254
- [22] Magee CL (1970) The nucleation of martensite. *Phase Trans* 3:115–116
- [23] Sano Y, Chang SN, Meyers MA, Nemat-Nasser S (1992) Identification of stress-induced nucleation sites for martensite in Fe–31.8 wt% Ni–0.02 wt% C alloy. *Acta Metall et Mater* 40(2):413–417
- [24] He BB, Xu W, Huang MX (2014) Increase of martensite start temperature after small deformation of austenite. *Mater Sci Eng A* 609:141–146

- [25] Song H, Hoyt JJ (2016) A molecular dynamics study of heterogeneous nucleation at grain boundaries during solid-state phase transformations. *Comput Mater Sci* 117:151–163
- [26] Kajiwaru S (1986) Roles of dislocations and grain boundaries in martensite nucleation. *Metall Mater Trans A* 17(10):1693–1702
- [27] Otte HM (1957) The formation of stacking faults in austenite and its relation to martensite. *Acta Metall* 5(11):614–627
- [28] Shimizu K, Oka M, Wayman CM (1970) The association of martensite platelets with austenite stacking faults in an Fe-8Cr-1C alloy. *Acta Metall* 18(9):1005–1011
- [29] Yang H-S, Bhadeshia HKDH (2009) Austenite grain size and the martensite-start temperature. *Scr Mater* 60(7):493–495
- [30] Hanamura T, Torizuka S, Tamura S, Enokida S, Takechi H (2013) Effect of austenite grain size on transformation behavior, microstructure and mechanical properties of 0.1C–5Mn martensitic steel. *ISIJ Int* 53(12):2218–2225
- [31] Celada-Casero C, Sietsma J, Santofimia MJ (2019) The role of the austenite grain size in the martensitic transformation in low carbon steels. *Mater Des* 167:107625
- [32] Nichol TJ, Judd G, Ansell GS (1977) The relationship between austenite strength and the transformation to martensite in Fe-10 pct Ni-0.6 pct C alloys. *Metall Mater Trans A* 8(12):1877–1883
- [33] Brofman PJ, Ansell GS (1983) On the effect of fine grain size on the Ms temperature in Fe-27Ni-0.025C alloys. *Metall Mater Trans A Phys Metall Mater Sci*. 14A(9):1929–1931
- [34] Glezer AM, Blinova EN, Pozdnyakov VA, Shelyakov AV (2003) Martensite transformation in nanoparticles and nanomaterials. *J Nanopart Res* 5:551–560
- [35] Takaki S, Fukunaga K, Junaidi S, Tsuchiyama T (2004) Effect of grain refinement on thermal stability of metastable austenitic steel. *Mater Trans* 45:2245–2251
- [36] Wang ZW, Wang YB, Liao XZ, Zhao YH, Lavernia EJ, Zhu YT, Horita Z, Langdon TG (2009) Influence of stacking fault energy on deformation mechanism and dislocation storage capacity in ultrafine-grained materials. *Scr Mater* 60(1):52–55
- [37] Frank M, Nene SS, Chen Y, Gwalani B, Kautz EJ, Devaraj A, An K, Mishra RS (2020) Correlating work hardening with co-activation of stacking fault strengthening and transformation in a high entropy alloy using in-situ neutron diffraction. *Sci Rep* 10(1):1–10
- [38] Hidalgo J, Santofimia MJ (2016) Effect of prior austenite grain size refinement by thermal cycling on the microstructural features of as-quenched lath martensite. *Metall Mater Trans A* 47(11):5288–5301
- [39] Waitz T, Tsuchiya K, Antretter T, Fischer FD (2009) Phase transformations of nanocrystalline martensitic materials. *MRS Bull* 34:814–821
- [40] Wu B-B, Wang Z-Q, Shang C-J, Yu Y-S, Misra D (2021) Nucleation analysis of variant transformed from austenite with Σ_3 boundary in high-strength low-alloy steel. *Acta Metall Sin-Engl* 34(4):523–533
- [41] Plimpton S (1995) Fast parallel algorithms for short-range molecular dynamics. *J Comput Phys* 117:1–19
- [42] Stukowski A (2010) Visualization and analysis of atomistic simulation data with OVITO- the Open Visualization Tool. *Model Simul Mater Sci Eng* 18(1):015012
- [43] Stukowski A (2012) Structure identification methods for atomistic simulations of crystalline materials. *Model Simul Mat Sci Eng* 20(4):045021
- [44] Larsen PM, Schmidt S, Schiøtz J (2016) Robust structural identification via polyhedral template matching. *Model Simul Mat Sci Eng* 24(5):055007
- [45] Hirel P (2015) AtomsK: a tool for manipulating and converting atomic data files. *Comput Phys Commun* 197:212–219
- [46] Engin C, Sandoval L, Urbassek HM (2008) Characterization of Fe potentials with respect to the stability of the bcc and fcc phase. *Model Simul Mat Sci Eng* 16(3):035005
- [47] Meiser J, Urbassek HM (2020) $\alpha \leftrightarrow \gamma$ phase transformation in iron: comparative study of the influence of the interatomic interaction potential. *Model Simul Mat Sci Eng* 28(5):055011
- [48] Meyer R, Entel P (1998) Martensite-austenite transition and phonon dispersion curves of studied by molecular-dynamics simulations. *Phys Rev B* 57(9):5140–5147
- [49] Cuppari MGDV, Veiga RGA, Goldenstein H, Silva JEG, Becquart CS (2017) Lattice instabilities and phase transformations in Fe from atomistic simulations. *J Phase Equilib Diffus* 38(3):185–194
- [50] Müller M, Erhart P, Albe K (2007) Analytic bond-order potential for bcc and fcc iron-comparison with established embedded-atom method potentials. *J Phys Condens Matter* 19(32):326220
- [51] Bleskov I, Hickel T, Neugebauer J, Ruban A (2016) Impact of local magnetism on stacking fault energies: a first-principles investigation for FCC iron. *Phys Rev B* 93:214115
- [52] Dick A, Hickel T, Neugebauer J (2009) The effect of disorder on the concentration-dependence of stacking fault energies in $\text{Fe}_{1-x}\text{Mn}_x$ - a first principles study. *Steel Res Int* 80(9):603–608
- [53] Wang B, Sak-Saracino E, Gunkelmann N, Urbassek HM (2014) Molecular-dynamics study of the $\alpha \leftrightarrow \gamma$ phase transition in Fe-C. *Comput Mater Sci* 82:399–404

- [54] Karewar S, Sietsma J, Santofimia MJ (2019) Effect of C on the martensitic transformation in Fe-C alloys in the presence of pre-existing defects: a molecular dynamics study. *Crystals* 9(2):99
- [55] Entel P, Meyer R, Kadau K, Herper HC, Hoffmann E (1998) Martensitic transformations: first-principles calculations combined with molecular-dynamics simulations. *Eur Phys J B* 5(3):379–388
- [56] Entel P, Meyer R, Kadau K (2000) Molecular dynamics simulations of martensitic transitions. *Philos Mag B* 80(2):183–194
- [57] Sandoval L, Urbassek HM, Entel P (2009) The bain versus Nishiyama–Wassermann path in the martensitic transformation of Fe. *New J Phys* 11(10):103027
- [58] Tripathi PK, Karewar S, Lo Y-C, Bhowmick S (2021) Role of interface morphology on the martensitic transformation in pure Fe. *Materialia* 16:101085
- [59] Pepperhoff W, Acet M. (2001) The influence of magnetism on the physical properties of iron alloys. In: *Constitution and Magnetism of Iron and its Alloys*. Engineering Materials. Springer, Berlin, Heidelberg
- [60] Sak-Saracino, E., Urbassek, H.M. (2015) Temperature-induced phase transformation of $\text{Fe}_{1-x}\text{Ni}_x$ alloys: molecular-dynamics approach. *Eur. Phys. J. B* 88:169
- [61] Rammo NN, Abdulah OG (2006) A model for the prediction of lattice parameters of iron-carbon austenite and martensite. *J Alloys Compd* 420(1):117–120
- [62] Lee B-J, Baskes MI, Kim H, Koo Cho Y (2001) Second nearest-neighbor modified embedded atom method potentials for bcc transition metals. *Phys Rev B* 64:184102
- [63] Song H, Hoyt J (2015) An atomistic simulation study of the crystallographic orientation relationships during the austenite to ferrite transformation in pure Fe. *Model Simul Mat Sci Eng* 23(8):085012
- [64] Rittner JD, Seidman DN, Merkle KL (1996) Grain-boundary dissociation by the emission of stacking faults. *Phys Rev B* 53:4241–4244
- [65] Ueda M, Yasuda HY, Umakoshi Y (2001) Effect of grain boundary character on the martensitic transformation in Fe-32at.%Ni bicrystals. *Acta Mater* 49(17):3421–3432
- [66] Chapter 5—formation of martensite. In: Bhadeshia H, Honeycombe R (eds.) *Steels: microstructure and properties* (Fourth Edition), pp 135–177. Butterworth-Heinemann (2017)
- [67] Abdullaev RN, Khairulin RA, Stankus SV (2020) Volumetric properties of iron in the solid and liquid states. *J Phys Conf Ser* 1675(1):012087
- [68] Burgers WG (1934) On the process of transition of the cubic-body-centered modification into the hexagonal-close-packed modification of zirconium. *Physica* 1(7):561–586
- [69] Verbeken K, Barbé L, Raabe D (2009) Evaluation of the crystallographic orientation relationships between FCC and BCC phases in TRIP steels. *ISIJ Int* 49(10):1601–1609
- [70] Song T, Cooman BCD (2014) Martensite nucleation at grain boundaries containing intrinsic grain boundary dislocations. *ISIJ Int* 54(10):2394–2403
- [71] Meiser J, Urbassek HM (2019) Influence of grain boundaries on the austenitic and martensitic phase transitions in iron. *Eur Phys J B* 92(2):1–7
- [72] Tanaka K, Oshima R (1991) Role of annealing twin in the formation of variant structure of bct martensite in Fe-Pd alloy. *Mater Trans JIM* 32(4):325–330
- [73] Pitsch W, Schrader A (1958) Die ausscheidungsform des ϵ -karbids im ferrit und im martensit beim anlassen. *Arch Eisenhüttenwes* 29:715–721
- [74] Greninger AB, Troiano AR (1940) Crystallography of austenite decomposition. *Trans AIME* 140:307–336
- [75] Lu L, Shen Y, Chen X, Qian L, Lu K (2004) Ultrahigh strength and high electrical conductivity in copper. *Science* 304(5669):422–426
- [76] Sun L, He X, Lu J (2018) Nanotwinned and hierarchical nanotwinned metals: a review of experimental, computational and theoretical efforts. *NPJ Comput Mater* 4(1):1–18

Publisher's Note Springer Nature remains neutral with regard to jurisdictional claims in published maps and institutional affiliations.